

# Phase Continuity, Brittle to Ductile Transition Temperature, and Creep Behavior of a Eutectic Mo–20Si–52.8Ti Alloy

Aditya Srinivasan Tirunilai, Frauke Hinrichs, Daniel Schliephake, Michael Engstler, Frank Mücklich, Susanne Obert, Georg Winkens, Alexander Kauffmann,\* and Martin Heilmaier\*

Mo–Si–Ti alloys, like eutectic Mo–20Si–52.8Ti (at%), have previously been intensely investigated, owing to their excellent oxidation and creep resistance. To better understand high-temperature mechanical behavior, a holistic assessment of microstructural features is necessary. Correspondingly, 3D-focused ion beam tomography is carried out in Mo–20Si–52.8Ti. The results indicate a severely interconnected network of Mo solid solution ( $\text{Mo}_{\text{SS}}$ ) and intermetallic  $(\text{Ti},\text{Mo})_5\text{Si}_3$ . Both phases retain similar network connectivity, lamellar sizes, etc. The brittle to ductile transition temperature (BDTT) is then determined through a series of bending tests and interpreted using the microstructural information. The BDTT is found to be  $\approx 1100\text{--}1150\text{ }^\circ\text{C}$ , different from Mo–9Si–8B with a continuous  $\text{Mo}_{\text{SS}}$  network. The BDTT is an immediate consequence of the continuous network of both  $\text{Mo}_{\text{SS}}$  and  $(\text{Ti},\text{Mo})_5\text{Si}_3$ . The  $\text{Mo}_{\text{SS}}$  network is instrumental in crack trapping and bridging, indicating that the present phase distribution maximized the mechanical performance over  $(\text{Ti},\text{Mo})_5\text{Si}_3$ . Having determined the network microstructure and BDTT, tensile creep behavior is evaluated and compared to previously published compressive creep results. The results show consistency in terms of strain rate, stress exponent, and microstructural features indicating a reliably good creep resistance for the network microstructure of Mo–20Si–52.8Ti regardless of loading direction.

## 1. Introduction


High-temperature applications require materials of a unique combination of low density, good oxidation resistance, and high-temperature strength. Ni-based super-alloys are extensively used for high-temperature structural applications since they possess this combination,<sup>[1,2]</sup> with high-temperature strength and creep resistance arising from the unique microstructures of A1 matrix and  $\text{L}_{12}$  precipitates. However, to further increase the application temperature, through which energy conversion efficiency would increase, new material systems need to be developed.<sup>[3]</sup> Refractory silicide alloys like Mo–Si–B alloys<sup>[4]</sup> have shown great potential in this regard.

For the past two and a half decades, Mo–Si–B alloys have been widely investigated as they possess excellent creep and oxidation resistance at temperatures up to  $1300\text{ }^\circ\text{C}$ , as dictated by phase constitution and volume fraction of intermetallic phases  $\text{Mo}_3\text{Si}$ ,  $\text{Mo}_5\text{Si}_3$ , and  $\text{Mo}_5\text{SiB}_2$ .<sup>[5,6]</sup> However, the oxidation resistance of these Mo–Si–B

alloys at intermediate temperatures below  $1000\text{ }^\circ\text{C}$  is insufficient.<sup>[7]</sup> At these temperatures,  $\text{MoO}_3$  is formed and subsequently evaporates, leading to the so-called “pecking” phenomenon.<sup>[8]</sup> The recent development of Mo–Si–Ti alloys has shown that pecking can be suppressed with sufficient Ti content.<sup>[7]</sup> Furthermore, the addition of Ti leads to a comparatively lower density, e.g.,  $6.2\text{ g cm}^{-3}$  for eutectic Mo–20Si–52.8Ti<sup>[9]</sup> (unless otherwise stated, all compositions are in at% throughout the article) compared to  $9.6\text{ g cm}^{-3}$  for Mo–9Si–8B.<sup>[10]</sup> Research has already been conducted on the 3D architecture<sup>[11]</sup> and corresponding effects on the brittle to ductile transition temperatures (BDTTs) of Mo–Si–B alloys.<sup>[12,13]</sup> It was found that the BDTT is dictated by: 1) the content of interstitial impurities like O,<sup>[14]</sup> 2) the Si content in Mo solid solution ( $\text{Mo}_{\text{SS}}$ ) and at grain boundaries,<sup>[15,16]</sup> 3) the volume fraction of the more ductile  $\text{Mo}_{\text{SS}}$ ,<sup>[12–14]</sup> and 4) the matrix character of disordered and intermetallic phases.<sup>[11,13]</sup> However, similar information does not exist for Mo–Si–Ti alloys and it, therefore, needs to be determined.

A. S. Tirunilai, F. Hinrichs, D. Schliephake, S. Obert, G. Winkens, A. Kauffmann, M. Heilmaier  
Institute for Applied Materials (IAM-WK)  
Karlsruhe Institute of Technology (KIT)  
Engelbert-Arnold-Str. 4, D-76131 Karlsruhe, Germany  
E-mail: alexander.kauffmann@kit.edu; martin.heilmaier@kit.edu

M. Engstler, F. Mücklich  
Department of Materials Science and Engineering  
Saarland University  
66123 Saarbrücken, Germany

 The ORCID identification number(s) for the author(s) of this article can be found under <https://doi.org/10.1002/adem.202200918>.

© 2022 The Authors. Advanced Engineering Materials published by Wiley-VCH GmbH. This is an open access article under the terms of the Creative Commons Attribution License, which permits use, distribution and reproduction in any medium, provided the original work is properly cited.

DOI: 10.1002/adem.202200918

While O content may be determined by carrier gas hot extraction, and this correspondingly affects Si segregation to grain boundaries, phase fraction, and distribution, to evaluate connectivity, is not easily determined through conventional microstructural analysis. Phase connectivity is crucial to identifying a matrix phase, which can only be effectively determined by 3D microstructural analysis,<sup>[17]</sup> as has been seen for some Mo–Si–B alloys.<sup>[11]</sup> The knowledge of the 3D microstructure is important as it would significantly affect high-temperature deformation as well as creep behavior.<sup>[12,13,18]</sup> To investigate a 3D volume of the Mo–20Si–52.8Ti, 3D focused ion beam (FIB) tomography was conducted. Subsequently, the BDTT was determined through a series of three-point bending tests. The 3D microstructure in combination with conventional micrographs of the deformed specimens was used to interpret the results of the bending tests.

To build on the results of the bending test, it should be ensured that the previously published compressive creep results can be reasonably extended to tensile creep as the practical application loading condition.<sup>[10]</sup> Correspondingly, creep in tension must be investigated and compared to creep in compression, as is presently done with tests carried out at 1200 and 1300 °C.

## 2. Experimental Section

Mo–20Si–52.8Ti (at%) was synthesized from bulk elemental pieces of Mo (99.5%), Ti (99.8%), and Si (99.99%). The elements were arc melted in a water-cooled Cu crucible in an Ar atmosphere. For further details on the arc melting process, please refer to ref. [19]. The cast samples were subsequently machined by electrical discharge machining (EDM) to obtain: 1) cuboids of dimensions  $10 \times 10 \times 5 \text{ mm}^3$  for 3D FIB-based tomography, 2) cuboids of dimensions  $3 \times 4 \times 45 \text{ mm}^3$  for BDTT tests, 3) cuboids of dimensions  $3 \times 3 \times 4.5 \text{ mm}^3$  for compressive creep testing, and 4) dog-bone specimens with gauge section dimensions  $3 \times 4 \times 20 \text{ mm}^3$  for tensile creep testing.

For FIB-based tomography, the  $10 \times 10 \text{ mm}^2$  surface of the cuboid was ground with SiC grinding papers of successively higher grades up to P2500 followed by polishing by 3 and 1  $\mu\text{m}$  diamond polishing suspension. They were finally polished using an oxide polishing suspension (OPS) of pH = 9.8 supplied by Struers. A  $125 \times 125 \times 125 \mu\text{m}^3$  volume at one of the edges of the specimen was designated as the region of interest (ROI) and a corresponding surface was coated with a protective 1  $\mu\text{m}$  thick Pt layer to suppress ion damage and curtaining effects.<sup>[20,21]</sup> A  $125 \times 125 \mu\text{m}^2$  area was analyzed via backscattered electron (BSE) imaging at 5 kV and 1.6 nA, after which a 150 nm layer was removed using the ion beam at 30 kV and 200 nA. This process was repeated, down to a depth of 125  $\mu\text{m}$  yielding the 3D microstructural information. The serial sectioning was carried out using Helios G4 PFIB Dual Beam System and Auto Slice and View G4 Software, both from Thermo Fisher Scientific. In the present case, preliminary 2D scanning electron microscope (SEM) imaging indicated that the smallest feature was  $<0.5 \mu\text{m}$  in size. To ensure sufficient feature resolution the voxel size was chosen as a cube with a side length of 150 nm. Segmentation noise and artifacts were eliminated utilizing morphological operations such as erosion and dilation as well

as manual corrections. Erosion consists of the elimination of the outermost voxels of a given phase. In the present case, four different erosion steps were carried out wherein 1–4 voxels were eroded and connectivity was correspondingly evaluated. 3D reconstruction visualization was done using the Thermo Fisher Avizo software package. The connectivity and additional quantitative analysis were done using the MAVI (Fraunhofer ITWM Kaiserslautern) software package.

Specimens for three-point bending tests and tensile creep were polished to the same level as stated above for FIB-based tomography while compressive creep specimens were prepared as stated in refs. [10,19]. The polished specimens were then tested in a Zwick Z100 with a Maytec high-temperature vacuum furnace. For the bending test, the two supporting pins were 40 mm apart with the external load being applied in the center. Bending tests were carried out at 50 K intervals between 900 and 1200 °C, with the load applied at a cross-head speed of  $0.01 \text{ mm s}^{-1}$ , which corresponds to a true strain rate of  $\approx 1 \times 10^{-4} \text{ s}^{-1}$  for the outer-most tensile fiber of the specimen. Creep tests were carried out at 1200 and 1300 °C, at loads of 50, 75, and 100 MPa true stress. The data acquired from bending and creep tests were processed using OriginPro 2019 from Origin Lab.

Deformed specimens from the bending and creep tests were investigated by SEM analysis carried out on an Apreo S LoVac from Thermo Fisher Scientific and an LEO EVO 50 by Zeiss. Fracture surfaces were investigated by secondary electron (SE) and BSE imaging while the deformed microstructure was analyzed by the latter.

## 3. Results and Discussion

### 3.1. Phase Continuity

**Figure 1** displays the color-coded microstructure of the eutectic alloy, consisting of the two phases  $\text{Mo}_{55}$  (Strukturbericht A2, W prototype, space group no. 229) and  $(\text{Ti},\text{Mo})_5\text{Si}_3$  (Strukturbericht D8<sub>8</sub>,  $\text{Mn}_5\text{Si}_3$ , space group no. 193) distributed as interspersed networks. The different phases were identified through Z-based contrast in BSE mode, as understood from chemical compositions determined previously.<sup>[7]</sup> The feature width estimated from this micrograph was  $(2.3 \pm 0.5)$  and  $(2.8 \pm 0.6) \mu\text{m}$  for  $\text{Mo}_{55}$  and  $(\text{Ti},\text{Mo})_5\text{Si}_3$ , respectively, as estimated by the linear intercept method. The corresponding phase boundary density was found to be  $(0.75 \pm 0.11) \mu\text{m}^{-1}$ , similar to the previously estimated  $(0.60 \pm 0.04) \mu\text{m}^{-1}$ .<sup>[8]</sup> The colored regions in **Figure 1b,c** depict  $\text{Mo}_{55}$  and  $(\text{Ti},\text{Mo})_5\text{Si}_3$ , respectively, wherein individual colonies (pixel-connected regions of the same BSE brightness) are distinguished by different colors. The relative phase fraction (**Table 1**) is consistent with previous observations, where no distinct inter-connected phase was identified via 2D microstructural analysis.

To analyze the microstructure in more detail and understand features like connectivity, 3D microstructural analysis is carried out through FIB-based tomography. The reconstructed  $125 \times 125 \times 125 \mu\text{m}^3$  volume distinguishing  $\text{Mo}_{55}$  and  $(\text{Ti},\text{Mo})_5\text{Si}_3$  phases are displayed in **Figure 2**. The 2D micrograph in **Figure 1** was taken from the volume reconstructed in

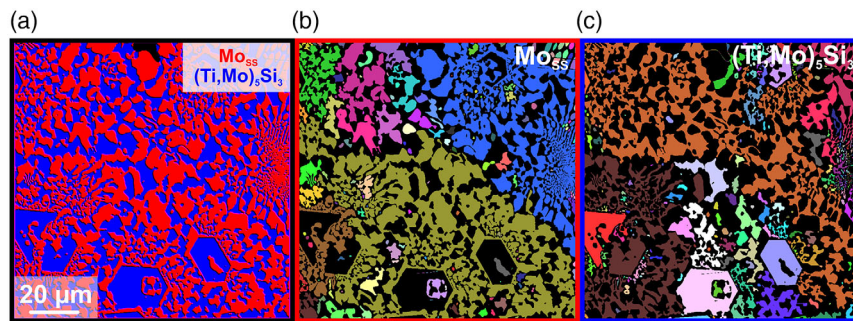


**Figure 1.** Color-coded BSE micrographs of: a) eutectic Mo–20Si–52.8Ti and colonies of: b) Mo<sub>SS</sub> and c) (Ti,Mo)<sub>5</sub>Si<sub>3</sub>. Figure 1a represents a phase map of Mo<sub>SS</sub> and (Ti,Mo)<sub>5</sub>Si<sub>3</sub> identified by red and blue, respectively. Figure 1b,c depicts pixel-connected regions of the same BSE brightness corresponding to Mo<sub>SS</sub> and (Ti,Mo)<sub>5</sub>Si<sub>3</sub>, respectively. The different colors in Figure 1b,c represent individual colonies disconnected from other colonies.

**Table 1.** Results of 2D and 3D microstructural analysis indicating phase fractions, relative fraction of isolated particles, and tortuosity.

Phase	Phase fraction 2D [vol%]	Phase fraction 3D [vol%]	Isolated fraction 3D [vol%]	Tortuosity 3D		
				x	y	z
Mo <sub>SS</sub>	54	54.4	0.1	1.0–1.2	1.0–1.2	1.0–1.1
(Ti,Mo) <sub>5</sub> Si <sub>3</sub>	45	45.4	0.1	1.0–1.2	1.0–1.2	1.0–1.2

Figure 2 implying a consistency of SEM scan parameters and comparability.

The majority of each phase is completely interconnected (in gray) while small isolated particles are highlighted in red (Figure 2b,c). Despite the results of 2D analysis, both phases appear to form intensely interconnected networks with only  $\approx 0.1$  vol% of each phase being isolated. However, parts of the network may be connected by a single voxel (side length 150 nm) in such an evaluation, which could be an artifact from the microstructural reconstruction. Alternatively, even if it is found not to be an artifact, the practical contribution of such small branches would be minimal to both mechanical properties and oxidation resistance. To quantify the fraction of interconnected phase, which could have a practical impact on mechanical behavior, the 3D microstructure was subjected to erosion transformations, described in the materials and methods section. As a result, the number of unconnected or isolated regions increases with a greater number of voxels eroded, leading to an isolated,

phase-specific, volume fraction of 12.4 vol% of Mo<sub>SS</sub>, and 8.8 vol% of (Ti,Mo)<sub>5</sub>Si<sub>3</sub> when eroding four voxels. This implies that eliminating branches of diameters  $\leq 1.2$   $\mu\text{m}$  still results in an interconnection of  $\approx 90$  vol% of both phases. Thus, the high connectivity in 3D is validated, especially considering that some of the lamellae in Figure 1 are only  $\approx 0.5$   $\mu\text{m}$  in width. The 3D microstructures and associated volumes of unconnected phases for different erosion conditions are illustrated in the supplementary material (Figure S1 and S2, Supporting Information).

As part of the 3D reconstruction analysis, the tortuosity of each phase in terms of arc chord ratio was analyzed. It was found to be low at  $\approx 1$ –1.2 (see Table 1), indicating almost direct pathways through the phases. Even though a high tortuosity is expected to be beneficial for oxidation resistance, the present eutectic alloy shows excellent peeling resistance in the temperature range of 800–1200 °C.<sup>[10]</sup> For all evaluated parameters, lamellar width, phase fraction, connectivity, and tortuosity, Mo<sub>SS</sub>, and (Ti,Mo)<sub>5</sub>Si<sub>3</sub> are found to be similar.

### 3.2. BDTT

The results of the three-point bending tests are used to construct a plot of plastic strain at fracture ( $\epsilon_{\text{plastic}}$ ) of the outer tensile fiber as a function of temperature. This is displayed alongside literature data for Mo–Si–B alloys<sup>[12,13]</sup> (three-point bending tests, at a cross-head speed of 0.01 mm s<sup>-1</sup>, on a specimen of cross-section  $3 \times 3.8$  mm<sup>2</sup> across 40 mm span) and a single crystal Ti<sub>5</sub>Si<sub>3</sub><sup>[22]</sup> (compression tests at a strain rate of  $1 \times 10^{-4}$  s<sup>-1</sup>, on specimen

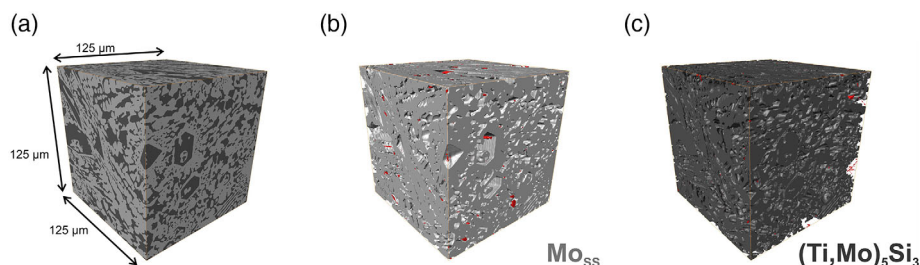


**Figure 2.** 3D microstructure reconstruction of a  $125 \times 125 \times 125$   $\mu\text{m}^3$  cube of a) eutectic Mo–20Si–52.8Ti, b) Mo<sub>SS</sub> and c) (Ti,Mo)<sub>5</sub>Si<sub>3</sub>. The regions colored in red indicate particles that are not connected to the phase network.

of dimensions  $1.5 \times 1.5 \times 4 \text{ mm}^3$ , respectively. BDTT is defined by the lowest temperature at which a finite plastic ductility was observed. In the case of eutectic specimens this is  $\approx 1100\text{--}1150 \text{ }^\circ\text{C}$ , in contrast to Mo–9Si–8B which shows a lower BDTT of  $950\text{--}1100 \text{ }^\circ\text{C}$ . Alternatively, single-crystalline  $\text{Ti}_5\text{Si}_3$ , exhibits the highest BDTT of  $\approx 1300 \text{ }^\circ\text{C}$ . BDTT for the eutectic alloy closely matches that of Mo–13Si–12B at  $1100\text{--}1200 \text{ }^\circ\text{C}$  as reported in refs. [12,13]. It should be noted that the single crystal ductility for  $\text{Ti}_5\text{Si}_3$  was evaluated based on compression test results and the corresponding orientation depicted in **Figure 3** has the lowest BDTT of all evaluated orientations.<sup>[22]</sup> Under practical conditions the BDTT for polycrystalline  $\text{Ti}_5\text{Si}_3$ , evaluated through bending or in tension would likely be even higher.

The eutectic alloy has a higher BDTT in comparison to Mo–9Si–8B despite the relatively similar volume fractions of ductile  $\text{Mo}_{\text{SS}}$  (51 vol% for Mo–9Si–8B<sup>[13]</sup> vs 54 vol% for Mo–20Si–52.8Ti). The difference in BDTT may be attributed to: 1) phase distribution, 2) O content, and/or 3) solute content of the  $\text{Mo}_{\text{SS}}$ . Although a relatively high interconnectivity of  $\text{Mo}_{\text{SS}}$  is established by 3D tomography, it does not represent a distinct matrix phase since  $(\text{Ti},\text{Mo})_5\text{Si}_3$  is also equally interconnected. This is in contrast to Mo–9Si–8B where the intermetallic phase is surrounded by a matrix of the more ductile  $\text{Mo}_{\text{SS}}$ , establishing that the matrix phase governs the BDTT in this case.<sup>[13]</sup> With respect to O, a greater O content was found to be detrimental to ductility as it results in the formation of  $\text{SiO}_2$  at phase boundaries, causing an embrittlement.<sup>[14]</sup> The relative O content presently measured by hot carrier gas extraction is found to be 49 wt ppm, in comparison to 100 wt ppm for Mo–9Si–8B.<sup>[14]</sup> The results thus imply that the O content does not play a major role in this comparison.

In the present case, the effect of dissolved Si and Ti in the solid solution needs to be considered. For a given material, the transition from ductile to brittle behavior is controlled by the relation of

stress needed to cause fracture (cleavage stress) and stress required to initiate plastic deformation (yield strength).<sup>[23]</sup> At lower temperatures, the former is lower so fracture takes place prior to yielding. As temperature increases, yield strength decreases due to thermal activation while cleavage stress exhibits a rather weak temperature dependence (similar to the decrease in elastic stiffness). Above BDTT, yielding can accordingly take place prior to fracture. When comparing pure Mo to  $\text{Mo}_{\text{SS}}$ , yield strength will increase due to solid solution strengthening and BDTT will increase as long as cleavage stress is considered approximately constant during alloying.

$\text{Mo}_{\text{SS}}$  in Mo–Si–B alloys is expected to have a Si content  $< 4 \text{ at}\%$  considering the solubility limit of Si in Mo,<sup>[24]</sup> while the Si content in  $\text{Mo}_{\text{SS}}$  of the eutectic alloy is 2.4 at%.<sup>[7]</sup> The comparably similar Si content might preclude any difference in BDTT from dissolved Si. The high Ti content ( $\approx 39\%$ ) in the eutectic alloy contributes to a substantial solid solution strengthening.<sup>[7]</sup> A significant lattice parameter change of  $\approx 6\%$  is achieved in this case (calculated as  $\frac{\Delta a}{a}$  using values from refs. [10,15]) leading to an increase of Vickers hardness from 196 HV0.1 for pure Mo up to 430 HV0.1 for Mo–40Ti, a binary solid solution similar to the one present in the eutectic alloy. However, while Ti content is not expected to have any inhomogeneous distribution in the microstructure or any other effect negative effect, Si can exhibit a negative influence in alternate ways, e.g., decrease of cleavage stress. As stated in ref. [15], Si additions tend to cause weakening of the grain boundaries resulting in easier intergranular crack propagation and potentially less ductility. Nevertheless, this negative effect may be mitigated in the present alloy for two reasons: 1) dissolved Si is low and in the range of  $\text{Mo}_{\text{SS}}$  in Mo–Si–B alloys, wherein a distinctly negative effect was not found, and 2) the present microstructure is a two-phase and fine-scaled where any excess Si can easily be trapped by  $(\text{Ti},\text{Mo})_5\text{Si}_3$  formation. On the basis of these points, the phase distribution is decisive for BDTT, whereas the influence of O content and dissolved species in the solid solution may be neglected in the present case.

Mo–13Si–12B exhibits brittle to ductile transition behavior similar to that of the eutectic alloy. This may be attributed to the intermetallic matrix found in this alloy, analogous to the severely interconnected network of  $(\text{Ti},\text{Mo})_5\text{Si}_3$  in the eutectic alloy. In contrast to the eutectic alloy and Mo–13Si–12B, single-crystalline  $\text{Ti}_5\text{Si}_3$  has an even higher BDTT. Krüger et al.<sup>[12,13]</sup> have pointed out that the matrix phase dictates the BDTT even for alloys of different phase fractions. Correspondingly, the lower BDTT presently observed for the eutectic alloy in comparison to single-crystalline  $\text{Ti}_5\text{Si}_3$  is due to the extensive  $\text{Mo}_{\text{SS}}$  network.

The fracture surfaces above and below the BDTT of the eutectic are as displayed in **Figure 4a,b**. At  $1000 \text{ }^\circ\text{C}$ , the surface appears to have undergone intraphase fracture, as the fracture surface is apparently flat across a colony of  $\text{Mo}_{\text{SS}}$  and  $(\text{Ti},\text{Mo})_5\text{Si}_3$ . While there are some smaller facets observed on the fracture surface of the specimen deformed at  $1150 \text{ }^\circ\text{C}$ , there appear to be indications of interphase fracture as many undulations of sizes in the range of the eutectic lamellae are observed. This transition from intra- to interphase fracture is typical of the greater toughness achieved at higher temperatures. This is because, at higher temperatures, the energy needed for crack propagation along

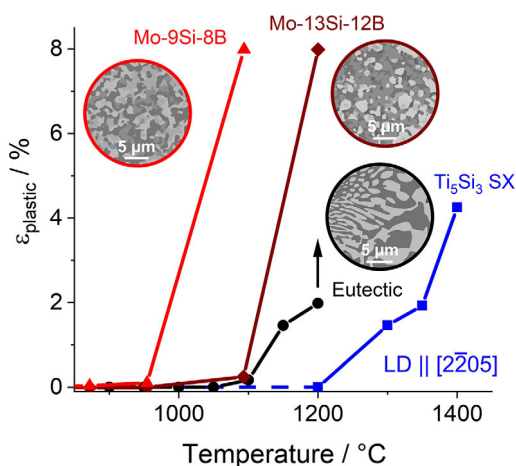


**Figure 3.** Plot of  $\epsilon_{\text{plastic}}$  versus  $T$  for the eutectic alloy, Mo–9Si–8B, Mo–13Si–12B, and single crystal  $\text{Ti}_5\text{Si}_3$  (estimated from compression tests) data in refs. [12,13,22]. The vertical black arrow indicates that the test was stopped prior to fracture. Circular insets display sketches of the microstructures for the eutectic alloy, Mo–9Si–8B and Mo–13Si–12B (the latter two according to ref. [12]).

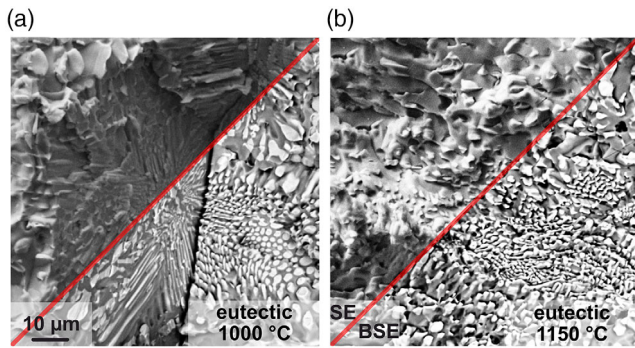


**Figure 4.** Fracture surfaces of samples subjected to bending test at: a) 1000 and b) 1150 °C. The top left half of the image depicts the secondary electron (SE) micrograph while the bottom right depicts the BSE micrograph and the two halves are separated by a red transparent diagonal. The scale bar is the same for both Figure 4a,b.

the phase boundary is lower than through the crystallite.<sup>[23]</sup> Correspondingly, at higher temperatures, the energy dissipation associated with crack propagation and therefore to achieve fracture along the interlacing phase boundary is higher than at lower temperatures where it may cut across a crystallite in direct pathways. The temperature separating these two behaviors is referred to as equicohesive temperature<sup>[23]</sup> and based on the present results, it is expected to be between 1000 and 1150 °C for the eutectic alloy. It should be noted that, owing to the longer crack propagation path, macroscopically measured strain may be greater, but the intrinsic ductility of the alloy is not necessarily higher at higher temperatures. The total energy required for crack propagation has increased and it is thus appropriate to state that at higher temperatures the toughness has improved.

Apart from the fracture surface, the specimen is metallographically prepared along a section perpendicular to the fracture surface, to depict the route of crack propagation (Figure 5). The crack propagates predominantly through the  $(\text{Ti},\text{Mo})_5\text{Si}_3$  following a circuitous path, deflected by  $\text{Mo}_{55}$ . In some regions, the crack appears along the  $\text{Mo}_{55}$  interface indicating a propensity for

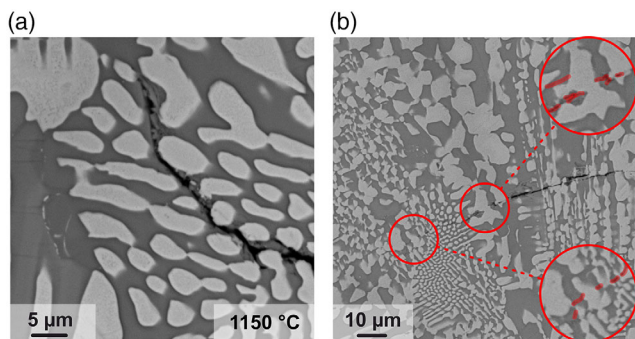


**Figure 5.** BSE micrographs of a metallographically prepared section indicating crack propagation for eutectic alloy tested at 1150 °C, where: a) depicts intragranular crack propagation through  $(\text{Ti},\text{Mo})_5\text{Si}_3$  and b) depicts crack propagation with insets showing crack bridging. The insets are identified by red circles and cracks are depicted by transparent red overlays within the insets.

interphase crack propagation as opposed to the intraphase crack propagation seen in  $(\text{Ti},\text{Mo})_5\text{Si}_3$ . While the crack transmits through  $(\text{Ti},\text{Mo})_5\text{Si}_3$ , it is trapped at the interface by ductile  $\text{Mo}_{55}$  in some cases (Figure 5b). Subsequently, the crack bridges across  $\text{Mo}_{55}$  continue on the other side of the ductile phase. Crack trapping and bridging is typical of multi-phase alloys with combinations of ductile and brittle phases, like in the Mo–Si–B system.<sup>[12,25]</sup> Solid solutions are able to deform more extensively than the intermetallic compounds. The localized dislocation activity in the ductile phase can cause crack formation in the adjacent brittle phase through slip transmission.<sup>[26,27]</sup> The regions showing crack propagation across both phases appear to have been displaced above and below the crack, likely a result of slip operation. These observations indicated that  $\text{Mo}_{55}$  crucially improves fracture toughness by mitigating the easy crack growth observed in  $(\text{Ti},\text{Mo})_5\text{Si}_3$ . As stated previously, despite  $\text{Mo}_{55}$  being the more ductile phase, the high Ti content contributes to substantial strengthening as seen by the significant hardness increase from pure Mo to Mo–40Ti.

### 3.3. Creep Behavior

To confirm that compressive creep behavior may be extended to tensile loading as the engineering load case of potential applications, tensile creep tests were carried out at 1200 and 1300 °C. The results illustrated in Figure 6 confirm macroscopic ductility during tensile loading and similar behavior under both loading conditions. It should be noted that in the case of both compressive and tensile creep, there exists a distinct minimum creep rate as opposed to an extended steady-state creep. These minimum creep rates are similar at 1200 °C with tensile creep rates  $\approx 1.9$  times that of the compressive creep rates as indicated in the Norton plot (Figure 6c). The stress exponents  $n$ , described by the relation

$$\dot{\epsilon}_{\min} \propto \sigma^n \quad (1)$$

are also similar with  $n = 3.2$  and  $3.7$  for tensile and compressive creep, respectively. At 1300 °C, the similarity between both loading directions is once again observed as minimum creep rates are similar within the resolution of the technique with  $n = 2.3$  and  $2.9$  for tensile and compressive creep loading, respectively. The stress exponents for experiments conducted at 1200 °C indicate dislocation-climb controlled creep as has been previously stated for compressive creep of the eutectic alloy.<sup>[10,19]</sup> The stress exponents at 1300 °C, however, lie in between characteristic values for dislocation-climb controlled and Nabarro–Herring creep or Coble creep, indicating some influence of diffusional creep.<sup>[28]</sup> Considering the higher diffusion rates at this temperature and the fine microstructure allowing for extensive boundary diffusion, this is to be expected.<sup>[29]</sup> However, there is still a significant contribution from dislocation activity, as indicated by the pronounced hardening in the transient creep regime. The slight difference in stress exponents may be considered a result of experimental scatter as demonstrated by the data for the compression creep tests conducted at 1200 °C and 100 MPa for six different tests.

To further compare the effect of tensile and compressive loading, a compressive creep test was interrupted at  $\approx 5\%$  strain and

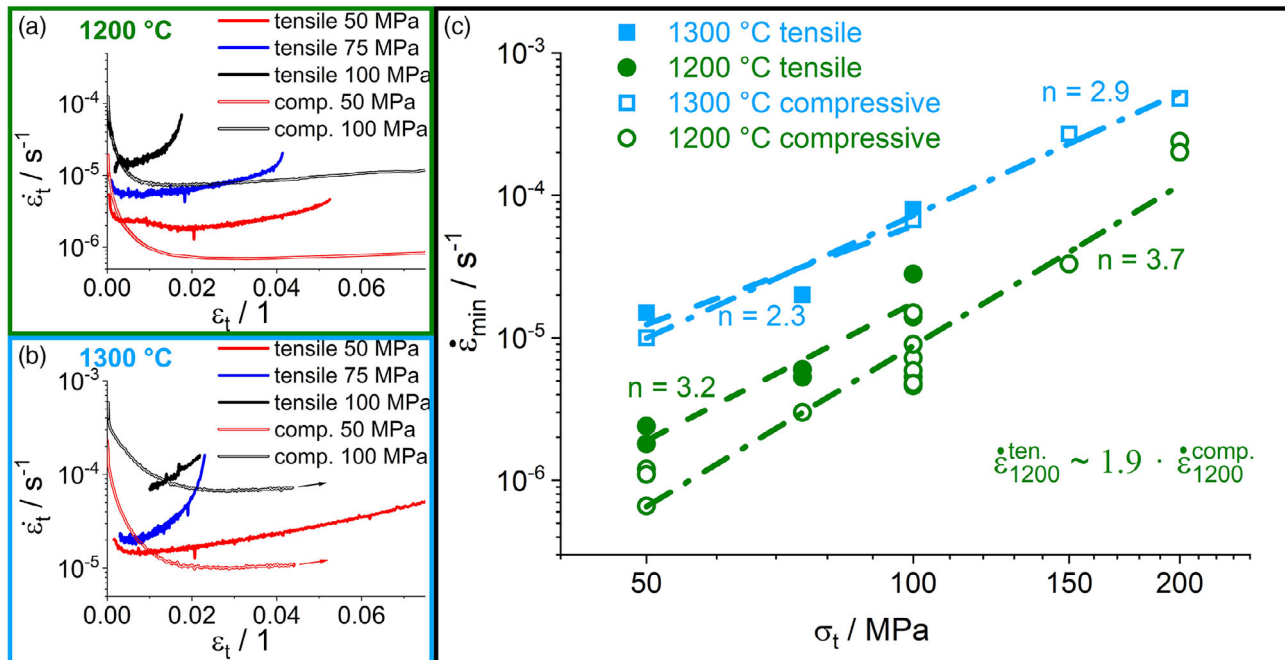


**Figure 6.** Plot of strain rate as a function of strain for the eutectic alloy tested in tension and compression at: a) 1200 °C and b) 1300 °C. c) Norton plot for compressive and tensile creep tests conducted at 1200 and 1300 °C. Compressive creep data taken from ref. [10]. Tensile creep data for some curves begin away from  $\epsilon_t = 0$ , as some strain was achieved during the load ramp to the respective stresses and only creep data for the associated stress value was considered.

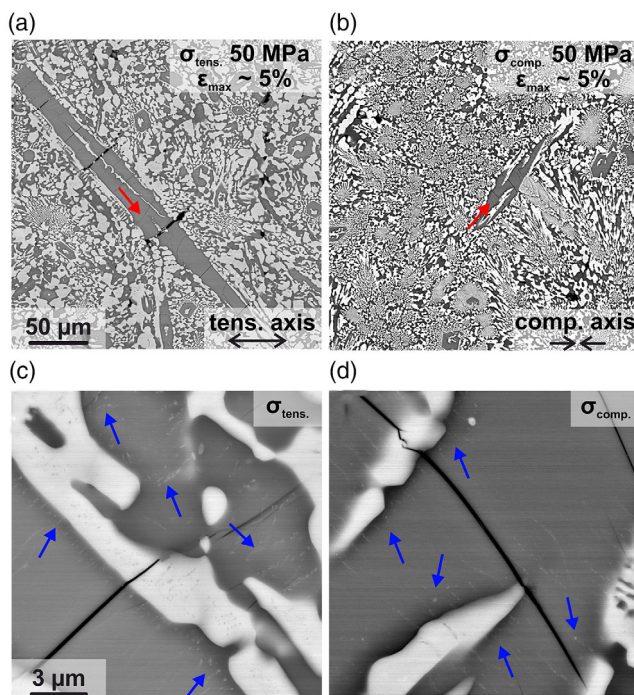


**Figure 7.** Microstructure of specimens subjected to creep at 1200 °C and 50 MPa in: a,c) tension and b,d) compression. The red arrows identify some of the cracks, while the blue arrows indicate  $\text{Mo}_{\text{SS}}$  precipitates in  $(\text{Ti},\text{Mo})_5\text{Si}_3$ .

the specimen was metallographically analyzed along with a tensile creep specimen of similar fracture strain, both loaded at 50 MPa. **Figure 7** identifies two features common under both loading conditions, namely: 1) cracks are seen propagating through the larger  $(\text{Ti},\text{Mo})_5\text{Si}_3$  region, oriented perpendicular to the longitudinal direction of the corresponding lamellae and 2) multiple Mo-rich precipitates are obtained in the  $(\text{Ti},\text{Mo})_5\text{Si}_3$  region. On closer inspection, it appears that these Mo-rich precipitates are formed close to the interface with lamellar  $\text{Mo}_{\text{SS}}$  and seem to extend perpendicularly to the longitudinal direction of the  $(\text{Ti},\text{Mo})_5\text{Si}_3$ .

$(\text{Ti},\text{Mo})_5\text{Si}_3$  undergoes a substantial change in the coefficient of thermal expansion (CTE)<sup>[30]</sup> with temperature while also being different from that of the adjacent  $\text{Mo}_{\text{SS}}$ .<sup>[7]</sup> This could already cause residual stress on cooling during the manufacturing of the alloy. The high anisotropy in CTE would additionally result in stress being accumulated in a single direction.<sup>[31]</sup> The residual stresses may result in easy crack formation in the larger volumes of  $(\text{Ti},\text{Mo})_5\text{Si}_3$  during creep testing. Some cracks have previously been identified in  $(\text{Ti},\text{Mo})_5\text{Si}_3$  of the manufactured material<sup>[7]</sup> as a result of CTE anisotropy. Nevertheless, the cracks observed in **Figure 7** propagate into the  $\text{Mo}_{\text{SS}}$  phase indicating that they are a result of creep deformation and not exclusively from CTE anisotropy.<sup>[31]</sup> Previous reports have estimated the creep exponents to be  $\approx 3$  in the temperature range 1000–1200 °C for  $\text{Ti}_5\text{Si}_3$ , characteristic of dislocation climb controlled creep.<sup>[30]</sup> The intense dislocation generation in this case could allow for enhanced diffusion while also providing nucleation sites for precipitates.<sup>[32]</sup> The arc melting process associated with rather high

cooling rates enables supersaturation of both phases with solute atoms. The thermodynamically stable phase mixture for the determined composition of  $(\text{Ti},\text{Mo})_5\text{Si}_3$ <sup>[7]</sup> in the eutectic alloy at 1200 °C is  $(\text{Ti},\text{Mo})_5\text{Si}_3$  ( $\approx 59$  vol%) +  $\text{Mo}_{\text{SS}}$  ( $\approx 41$  vol%), as estimated from PANDAT 2019 with PanMo database and crystallographic parameters determined in refs. [10,19,33]. This is the likely reason why  $\text{Mo}_{\text{SS}}$  precipitates nucleate in the  $(\text{Ti},\text{Mo})_5\text{Si}_3$  phase. Some crack trapping is obtained as indicated in Figure 7, but larger cracks appear to transmit through the phases. The direction of slip and subsequent crack propagation through  $\text{Mo}_{\text{SS}}$  is guided by their respective slip systems.

Previous reports have investigated mechanical behavior and creep of materials where only one of the phases undergoes significant deformation.<sup>[18,34]</sup> In such cases, the presence of a network structure: 1) can accommodate greater load,<sup>[18,34]</sup> 2) can partition load effectively,<sup>[18]</sup> and 3) corresponds to an improvement in long-term creep performance.<sup>[18,35]</sup> However, in the present case, both phases appear to exhibit plastic deformation, so the true impact of 3D microstructure is not yet clear. For further clarification future work has to be considered with transmission electron microscope (TEM) of the deformed microstructure but that is out of the scope of present work. This work will also be able to clarify the direction of crack propagation as it transmits across phases.

#### 4. Summary

The present article investigates the 3D microstructure of eutectic Mo–20Si–52.8 and correlates it to high-temperature mechanical properties. The key findings are as follows:

The 3D microstructure of the eutectic Mo–20Si–52.8 alloy consists of intensely interconnected networks of  $\text{Mo}_{\text{SS}}$  and  $(\text{Ti},\text{Mo})_5\text{Si}_3$ . Both phases are very similar in network connectivity, lamellar widths, tortuosity, and phase fraction.

The BDTT for the eutectic alloy is 1100–1150 °C. This temperature is in between the BDTT of alloys with  $\text{Mo}_{\text{SS}}$  matrix and monolithic intermetallic  $\text{Ti}_5\text{Si}_3$ , likely due to the alloy having a network of both  $\text{Mo}_{\text{SS}}$  and  $(\text{Ti},\text{Mo})_5\text{Si}_3$ . Crack trapping and crack bridging are observed as a result of the ductile  $\text{Mo}_{\text{SS}}$ .

Tensile and compressive creep behavior in the eutectic alloy is similar, in terms of creep rate, stress exponent, and microstructure. This indicates a consistency of active mechanisms regardless of loading direction with the high creep resistance being attributed to the excellent network structure.

#### Supporting Information

Supporting Information is available from the Wiley Online Library or from the author.

#### Acknowledgements

Financial support from the Deutsche Forschungsgemeinschaft (DFG) in the framework of grant no. HE 1872/33-2 and GRK 2561 MatCom-ComMat are gratefully acknowledged.

Open Access funding enabled and organized by Projekt DEAL.

#### Conflict of Interest

The authors declare no conflict of interest.

#### Data Availability Statement

The data that support the findings of this study are available from the corresponding author upon reasonable request.

#### Keywords

brittle to ductile transition, Mo–Si–Ti, tensile creep, 3D microstructure

Received: June 24, 2022

Revised: August 29, 2022

Published online:

- [1] D. Furrer, H. Fecht, *JOM* **1999**, 51, 14.
- [2] R. Darolia, *JOM* **1991**, 43, 44.
- [3] J. H. Perepezko, *Science* **2009**, 326, 1068.
- [4] P. Jain, K. S. Kumar, *Acta Mater.* **2010**, 58, 2124.
- [5] J. A. Lemberg, R. O. Ritchie, *Adv. Mater.* **2012**, 24, 3445.
- [6] V. Supatarawanich, D. R. Johnson, C. T. Liu, *Mater. Sci. Eng. A* **2003**, 344, 328.
- [7] S. Obert, A. Kauffmann, S. Seils, S. Schellert, M. Weber, B. Gorr, H.-J. Christ, M. Heilmaier, *J. Mater. Res. Technol.* **2020**, 9, 8556.
- [8] A. J. Thom, E. Summers, M. Akinc, *Intermetallics* **2002**, 10, 555.
- [9] P. Jéhanno, M. Heilmaier, H. Kestler, *Intermetallics* **2004**, 12, 1005.
- [10] D. Schliephake, A. Kauffmann, X. Cong, C. Gombola, M. Azim, B. Gorr, H.-J. Christ, M. Heilmaier, *Intermetallics* **2019**, 104, 133.
- [11] O. Hassomeris, G. Schumacher, M. Krüger, M. Heilmaier, J. Banhart, *Intermetallics* **2011**, 19, 470.
- [12] M. Krüger, S. Franz, H. Saage, M. Heilmaier, J. H. Schneibel, P. Jéhanno, M. Böning, H. Kestler, *Intermetallics* **2008**, 16, 933.
- [13] M. Krüger, P. Jain, K. S. Kumar, M. Heilmaier, *Intermetallics* **2014**, 48, 10.
- [14] M. Krüger, D. Schliephake, P. Jain, K. S. Kumar, G. Schumacher, M. Heilmaier, *JOM* **2013**, 65, 301.
- [15] D. Sturm, M. Heilmaier, J. H. Schneibel, P. Jéhanno, B. Skrotzki, H. Saage, *Mater. Sci. Eng. A* **2007**, 463, 107.
- [16] H. Saage, M. Krüger, D. Sturm, M. Heilmaier, J. H. Schneibel, E. George, L. Heatherly, C. Somsen, G. Eggeler, Y. Yang, *Acta Mater.* **2009**, 57, 3895.
- [17] A. Kruglova, M. Engstler, G. Gaiselmann, O. Stenzel, V. Schmidt, M. Roland, S. Diebels, F. Mücklich, *Comput. Mater. Sci.* **2016**, 120, 99.
- [18] G. Requena, G. Garcés, Z. Asghar, E. Marks, P. Staron, P. Cloetens, *Adv. Eng. Mater.* **2011**, 13, 674.
- [19] S. Obert, A. Kauffmann, M. Heilmaier, *Acta Mater.* **2020**, 184, 132.
- [20] M. Engstler, S. Mayer, C. Pauly, H. Clemens, F. Mücklich, *Adv. Eng. Mater.* **2013**, 15, 1125.
- [21] F. Lasagni, A. Lasagni, M. Engstler, H. P. Degischer, F. Mücklich, *Adv. Eng. Mater.* **2008**, 10, 62.
- [22] K. Kishida, M. Fujiwara, H. Adachi, K. Tanaka, H. Inui, *Acta Mater.* **2010**, 58, 846.
- [23] G. E. Dieter, *Mechanical Metallurgy*, McGraw-Hill Education (India), New Delhi **1986**.
- [24] A. B. Gokhale, G. J. Abbaschian, *JPE* **1991**, 12, 493.
- [25] J. J. Kruzic, J. H. Schneibel, R. O. Ritchie, *Scr. Mater.* **2004**, 50, 459.

- [26] A. Misra, R. Gibala, *Metall. Mater. Trans. A* **1997**, 28, 795.
- [27] A. Misra, Z. L. Wu, M. T. Kush, R. Gibala, *Mater. Sci. Eng. A* **1997**, 239–240, 75.
- [28] M. E. Kassner, *Fundamentals of Creep in Metals and Alloys*, Elsevier, Amsterdam **2009**.
- [29] G. B. Kale, R. V. Patil, *Mater. Trans.* **1994**, 35, 439.
- [30] R. Rosenkranz, G. Frommeyer, W. Smarsly, *Mater. Sci. Eng. A* **1992**, 152, 288.
- [31] J. J. Williams, M. J. Kramer, M. Akinc, *J. Mater. Res.* **2000**, 15, 1780.
- [32] D. A. Porter, K. E. Easterling, M. Y. Sherif, *Phase Transformations in Metals and Alloys*, CRC Press, Boca Raton, FL **2009**.
- [33] J. L. Murray, *Bull. Alloy Phase Diagr.* **1981**, 2, 185.
- [34] G. Requena, G. Garcés, M. Rodríguez, T. Pirling, P. Cloetens, *Adv. Eng. Mater.* **2009**, 11, 1007.
- [35] G. C. Requena, P. Degischer, E. D. Marks, E. Boller, *Mater. Sci. Eng. A* **2008**, 487, 99.